Numerical study on the dynamics of *Z*-pinch carbon plasma

K. T. Lee, S. H. Kim, D. Kim,[a] and T. N. Lee
Physics Department, Pohang Institute of Science and Technology, San 31 Hyoja-Dong, Nam Ku, Pohang, Kyungbuk, 790-784, Korea

(Received 22 August 1995; accepted 4 December 1995)

The dynamics of *Z*-pinch carbon plasma has been investigated using one-dimensional Lagrangian code. This code calculates the single-fluid, two-temperature magnetohydrodynamic (MHD) equations coupled with an ionization balance equation. The motion of plasma column and shock front is studied in comparison with the analytical models such as the snowplow and the slug model. The energy flow during the pinch is also studied. During the pinch phase, the temperature increases due to shock heating and adiabatic heating. After the pinch the plasma is cooled down rapidly due to adiabatic expansion which can lead to an adequate condition for recombination Extreme-Ultra-Violet (XUV) lasers. The effect of the radiative trapping of resonance line on hydrodynamics and population kinetics is also investigated. The calculation shows that there can exist a high gain on hydrogen-like C VI Balmer-α line (18.2 nm). © *1996 American Institute of Physics.* [S1070-664X(96)02203-1]

I. INTRODUCTION

Z-pinch plasma has attracted researchers for decades due to its copious x-ray radiation. The interest in the physics of *Z*-pinch plasma and its application to the lithography and microscopy has increased research activities.[1] There have been several analytical models suggested to describe the dynamics of *Z*-pinch plasma. The snowplow model describing the motion of plasma column, which was suggested by Rosenbluth,[2] predicts pinch time and its dependence on plasma parameters. But this model is not adequate to describe the behavior of plasma after pinch. Later, Miyamoto derived the snowplow energy equation[3] from the energy equation of the fluid equation. This model takes into account kinetic energy, internal energy and magnetic energy in the plasma. Using the snowplow energy equation, the reflection of plasma column can be described but the prediction of pinch time becomes less accurate than using the original snowplow model. On the other hand, the slug model[4] constructed by using the Rankine-Hugoniot conditions[5] and the adiabatic law is capable of describing the motion of shock front and the profiles of density and temperature. Even though the physics of *Z*-pinch plasma has been better understood in the past, the inherent complexity still requires further investigation. Duston and Duderstadt have studied *Z*-pinch helium plasma using one-dimensional magnetohydrodynamic (MHD) code.[6] The code solves two-temperature fluid equations and detailed collisional-radiative model equations, yielding the spatial profiles of density and temperature. The diffusion of magnetic field was also studied. Maxon and Wainwright[7] used the average ion model to evaluate the level populations of argon plasma. The comparison of simulated emission spectra with experimental data was made. Shlyaptsev[8] used a numerical simulation for the estimation of gain in a fast capillary discharge argon plasma. Numerical analysis is not only necessary and useful for the study of the dynamics but also helps to guide intended experiments.

In this paper, the dynamics of the *Z*-pinch carbon plasma using one-dimensional MHD code is presented. This code solves single-fluid, two-temperature fluid equations in the cylindrical geometry. This code includes the ionization balance equation which calculates the population of the ground states in each ionization stage. In the energy equation, heat conduction, Joule heating, Bremsstrahlung radiation and ion shock heating are included. The energy transfer during the ionization and recombination process is also considered. The energy loss due to the strong radiation from the resonance line is also taken into account.

The dynamics of *Z*-pinch plasma can be briefly described as initial Joule heating, shock heating just before a pinch, additional adiabatic heating with strong radiation loss and then rapid cooling by adiabatic expansion. The simulation also indicates that the rapid cooling of the plasma after implosion can provide adequate conditions for recombination Extreme-Ultra-Violet (XUV) lasers.[9] The gain calculation for hydrogen-like (H-like) C VI Balmer-α line (18.2 nm) in a *Z*-pinch carbon plasma shows a very high gain value, $G \simeq 20 \quad \mathrm{cm}^{-1}$ in an optically thin case. The effect of the reabsorption of Lyman-α line is also investigated, using the anomaly factor and the escape probability method. Even though the opacity can change gain drastically, the simulation still suggests that the gain can exist for adequate plasma parameters.

The gain of 2.8 cm^{-1} on 18.2 nm has been demonstrated in a capillary-discharge carbon plasma.[10] The condition of high temperature and density near the pinch is also suitable for the collisional-excitation pumping scheme of soft x-ray laser, which has recently been well demonstrated in Ne-like Ar plasma.[11]

II. FLUID MODEL

To study the dynamics of a *Z*-pinch plasma, the one-dimensional single-fluid, two-temperature MHD equations in the cylindrical geometry are adopted. In these equations, Joule heating, shock heating, Bremsstrahlung radiation, heat conduction and magnetic field diffusion are included. The

[a]Electronic mail: kimd@vision.postech.ac.kr

 1070-664X/96/3(4)/1340/8/$10.00

power losses due to various atomic processes are also included along with the calculation of the population of the ground state of each ionization stage. In this one-dimensional model, all variables are assumed to depend only on radial position, r, and for fluid velocity $\vec{v}=v(r)\hat{r}$, and for magnetic field $\vec{B}=B(r)\hat{\varphi}$. The MHD equations in the cylindrical coordinate including the ionization balance equation have the following forms in cgs unit.

The continuity equation (mass conservation) reads

$$\frac{d}{dt}N_i+\frac{N_i}{r}\frac{\partial}{\partial r}(rv)=0, \tag{1}$$

where $d/dt=\partial/\partial t+v(\partial/\partial r)$, N_i the ion density and v the fluid velocity in the radial direction.

The momentum equation is given by

$$m_iN_i\frac{d}{dt}v=-\frac{\partial}{\partial r}(N_eT_e+N_iT_i)-\frac{B}{4\pi r}\frac{\partial}{\partial r}(rB)-2\frac{v}{r}\frac{\partial}{\partial r}\chi+\frac{\partial}{\partial r}\left(\frac{4}{3}\frac{\chi}{r}\frac{\partial}{\partial r}(rv)\right), \tag{2}$$

where m_i is the ion mass, N_e the electron density, T_e, T_i the electron and ion temperature, respectively, and B the magnetic field induced by the axial plasma current. The first and second terms in the right-hand side of Eq. (2) are the thermal and magnetic pressure, respectively; the last two terms are the shock pressure using tensor form and χ is the shock viscosity given by[12]

$$\chi=\begin{cases}\dfrac{c_q}{2}l^2m_iN_i\dfrac{1}{r}\left|\dfrac{\partial}{\partial r}(rv)\right|, & \left(\dfrac{\partial v}{\partial r}\right)<0,\\ 0, & \left(\dfrac{\partial v}{\partial r}\right)>0,\end{cases} \quad (\mathrm{g\ cm^{-1}s^{-1}}),$$

where c_q is a constant to control the shock region.

The energy balance for electrons is described by

$$\frac{d}{dt}T_e=-\frac{2}{3}T_e\frac{1}{r}\frac{\partial}{\partial r}(rv)+\frac{2}{3}\frac{1}{N_er}\frac{\partial}{\partial r}\left(\kappa_{e\perp}r\frac{\partial}{\partial r}T_e\right)+\frac{2}{3}\frac{1}{N_e}(P_J-P_{brem}-P_{atom})-P_{ei}. \tag{3}$$

The first term is the energy loss due to the volume expansion (P_{exp_e}), the second the heat conduction (P_{cond_e}) and $\kappa_{e\perp}$ the electron heat conductivity perpendicular to the magnetic field;[13] P_J is Joule heating given by

$$P_J=\eta_\perp\left[\frac{c}{4\pi}\frac{1}{r}\frac{\partial}{\partial r}(rB)\right]^2$$

where $\eta_\perp$ is the plasma resistivity;[14] P_{brem} is the power loss due to Bremsstrahlung radiation.[15] The energy losses due to atomic processes include the loss due to the resonance line radiation and the collisional ionization and the heating by the recombination: $P_{atom}=P_{rad}+P_{ioniz}-P_{recomb}$ where

$$P_{rad}=\sum_{z=1}^{nz-1}N_eN_zS_{01}^z\epsilon_z\frac{A_{10}^z}{A_{10}^z+N_eS_{10}^z},$$

$$P_{ioniz}=\sum_{z=1}^{nz-1}N_eN_zR_z\chi_z,$$

$$P_{recomb}=\sum_{z=2}^{nz}N_eN_z\alpha_z\chi_z,$$

where N_z is the ion density of charge z, A_{10}^z the radiative decay rate of the resonance line of the z-th ionization stage having the largest A value[16]; S_{01}^z and S_{10}^z are the rate coefficients of collisional excitation and de-excitation between the levels, respectively,[9] and ϵ_z their energy difference. Here, R_z, α_z are the ionization and recombination rate coefficient, respectively.[17] In the calculation of P_{rad}, the collisional de-excitation process is considered since it becomes significant at high density. The last term in Eq. (3), P_{ei} is the energy equilibration between electron and ion, $P_{ei}=(T_e-T_i)/\tau_{eq}$, where τ_{eq} is the electron-ion equilibration time.[15]

The energy balance for ions is governed by

$$\frac{d}{dt}T_i=-\frac{2}{3}T_i\frac{1}{r}\frac{\partial}{\partial r}(rv)+\frac{2}{3}\frac{1}{N_ir}\frac{\partial}{\partial r}\left(\kappa_{i\perp}r\frac{\partial}{\partial r}T_i\right)+\frac{2}{3}\frac{\chi}{N_i}\left[\frac{1}{3}\left(\frac{1}{r}\frac{\partial}{\partial r}(rv)\right)^2+\left(r\frac{\partial}{\partial r}\left(\frac{v}{r}\right)\right)^2\right]+P_{ei}, \tag{4}$$

where $\kappa_{i,\perp}$ is the perpendicular ion heat conductivity[13] and the terms with χ represent the ion shock heating.

The magnetic field transport and diffusion equation reads

$$\frac{d}{dt}B=-B\frac{\partial}{\partial r}(v)+\frac{\partial}{\partial r}\left(\frac{c^2}{4\pi}\frac{\eta_\perp}{r}\frac{\partial}{\partial r}(rB)\right). \tag{5}$$

This equation is obtained using Maxwell equations and generalized Ohm's law neglecting the time variation of the electric field.[18]

The ground state population, N_z of the z-th ionization stage is calculated using the following ionization-balance equation,[9]

$$\frac{d}{dt}N_z=-N_eN_z\alpha_z-N_eN_zR_z+N_eN_{z+1}\alpha_{z+1}+N_eN_{z-1}R_{z-1}. \tag{6}$$

III. NUMERICAL METHOD

The Lagrangian scheme[19] is adopted for the numerical integration of the one-dimensional fluid equations described in the previous section. Since the integrations are performed following the fluid cells in this scheme, the continuity equation is changed to $(d/dt)\int_{\delta r}N_irdr=0$ and then the position of each fluid cell evolves as $(d/dt)r=v$. This Lagrangian scheme is adequate for Z-pinch system in which the plasma is compressed by magnetic pressure. The Crank-Nicholson type implicit scheme[19] is used to convert the differential equations into finite difference equations. For the convenience of constructing the difference equations, v is defined on the integral spatial-grid points and other variables on the half-integral ones. For the temporal evolution, all variables

are defined on the integral temporal-grid points. To avoid numerical instability, the size of time step, dt, is calculated at each time step using the following criterion,[18]

$$dt = c_1 Min\left\{\left(\Delta r \sqrt{\frac{m_i N_i}{N_e T_e + N_i T_i + (B^2/4\pi)}}\right)_j\right\},$$

where the subindex j represents a spatial-grid point, c_1 is a constant used as a safety factor and Min means the choice of the minimum value among the values in the curl bracket. The difference equations are then solved using Thomas algorithm[19] with appropriate boundary conditions. The boundary conditions at axis are

$$\left[\frac{\partial}{\partial r} T_e\right]_{r=0} = \left[\frac{\partial}{\partial r} T_i\right]_{r=0} = 0,$$

$$B(0) = 0,$$

$$v(0) = 0,$$

due to axial symmetry. No particle moves through the plasma-vacuum interface, r_p (the outer boundary). This is represented by the following conditions:[20]

$$\left[\frac{\partial}{\partial r} T_e\right]_{r=r_p} = \left[\frac{\partial}{\partial r} T_i\right]_{r=r_p} = 0,$$

$$\left[\frac{4}{3}\chi\left(\frac{\partial}{\partial r} v - \frac{1}{2}\frac{v}{r}\right) - (N_e T_e + N_i T_i)\right]_{r=r_p} = 0.$$

The vacuum density is specified as 3.5×10^8 cm^{-3} at the outer boundary. The magnetic field at the outer boundary is calculated using an external driving current, $I(t)$, instead of solving a circuit equation,

$$B(r_p) = \frac{2}{c}\frac{I}{r_p},$$

$$I(t) = I_0 \sin(\omega t).$$

To treat the nonlinear dependence of the transport coefficients the iteration method is adopted. The evaluation of the ionization balance equations is carried out using the method suggested by Carolan and Piotrowicz[21] which involves an eigenvalue problem.

IV. RESULTS AND DISCUSSIONS

For the simulation discussed in this paper, $I_0 = 340$ kA and $2\pi/\omega = 4$ μs are used, which are the values typically used in our laboratory. Initially, the plasma is assumed to be uniformly distributed with $N_e = N_i = 3.5\times 10^{17}$ cm^{-3}, $T_e = T_i = 1$ eV and $v = 0$ and the initial radius of $r_0 = 1.4$ cm.

The dynamics of *Z*-pinch plasma can be described by the balance between the thermal pressure and the magnetic pressure so-called magnetic piston. When the magnetic pressure is larger than the thermal pressure, the plasma is compressed inwardly onto the axis. As the plasma is compressed, the plasma becomes hotter due to Joule and shock heating and the thermal pressure increases. When the thermal pressure balances the magnetic pressure the plasma becomes stagnated and then expands. The important parameters characterizing the behavior are the time when the pinch occurs, the temperature to which the plasma is heated and the size of the plasma column to which the plasma is contracted. These are shown in Fig. 1. The simulation result is also compared with the snowplow model [Fig. 1(a)] and the slug model [Fig. 1(b)].

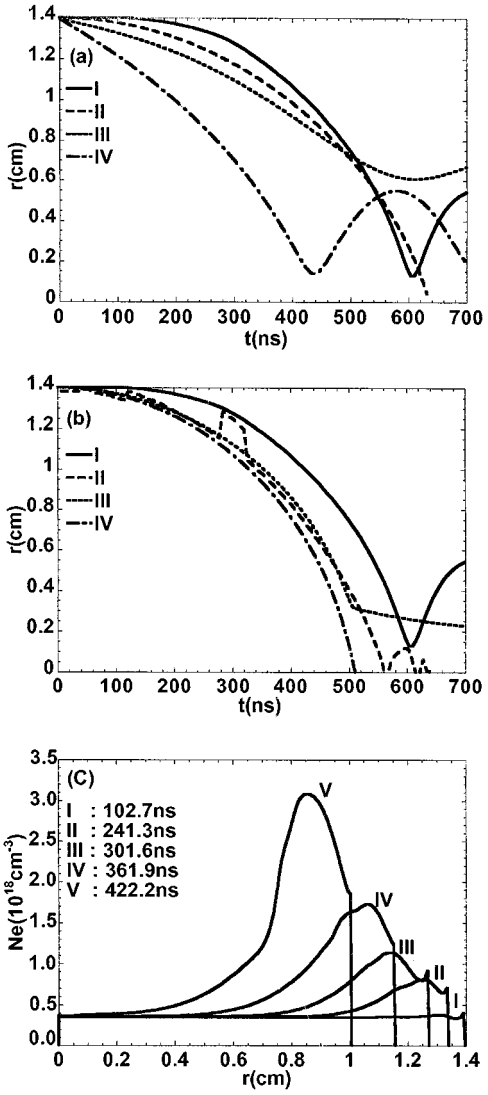

FIG. 1. The change of the positions of the plasma boundary and the shock front with respect to time. In (a) the motion of plasma boundary, r_p, by the simulation is compared with the prediction by the original snowplow model and the snowplow energy model [I: the simulation, II: the original snowplow model, III, IV: the snowplow energy model with $p_0 = -0.12$ and -0.32, respectively, where p_0 is the initial p value for the evaluation of the snowplow energy equation ($p = dx/d\tau$, $x = (r_p/r_0)^2$, $\tau = t/t_c$ and $t_c = (cr_0/2I_0)\sqrt{M_0}$)]. In (b) the simulation results for the motion of plasma boundary r_p and shock front r_s are compared with the predictions by the slug model [I: r_p, II: r_s from simulation; III: r_p, IV: r_s from the slug model]. In (c) the spatial distribution of electron density in compressional phase is shown, from which the appearance of shock and the accumulation of particle in boundary region can be noticed.

In the snowplow model,[2] the pinch time, τ_p, is estimated to be

$$\tau_p = 1.4\sqrt{\frac{cr_0}{\omega I_0}} M_0^{1/4},$$

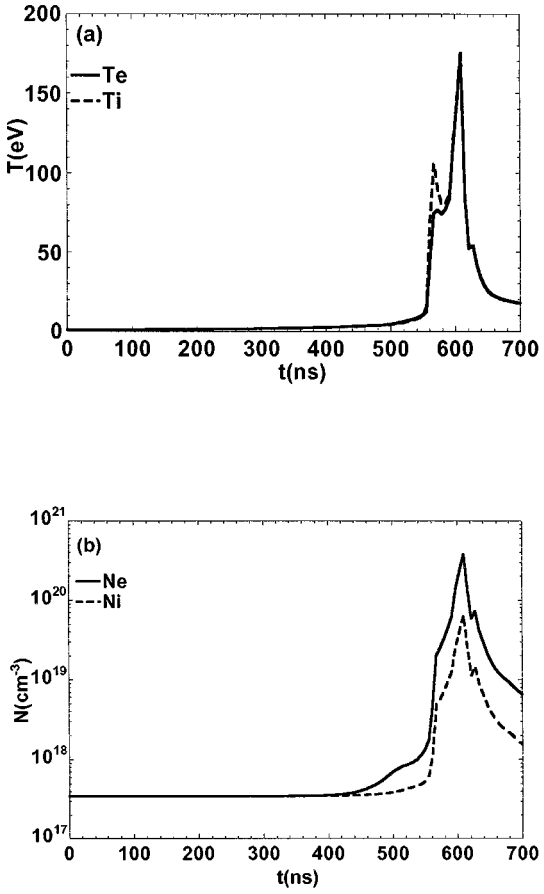

FIG. 2. The temporal variations of the electron and ion (a) temperature and (b) density at axis.

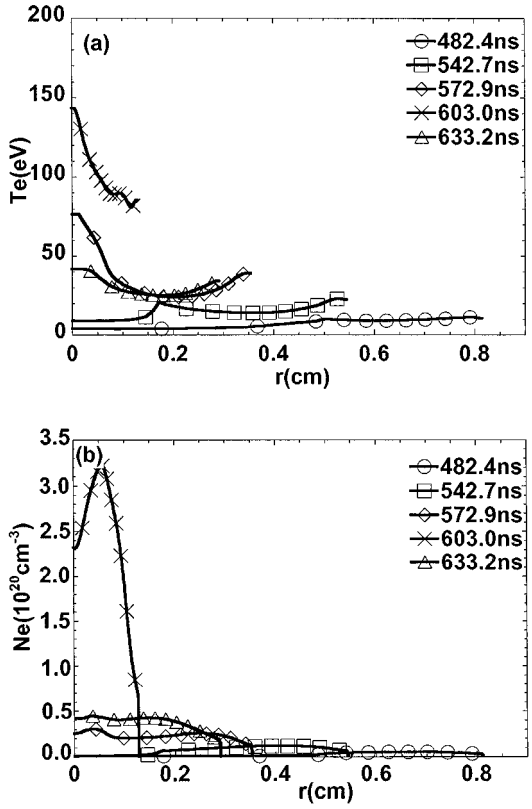

FIG. 3. The spatial distributions of (a) the electron temperature and (b) density for various times.

where r_0 is the initial radius, $2\pi/\omega$ the period of plasma current, I_0 the peak plasma current and M_0 the line mass density. For our simulation conditions, this formula yields $\tau_p = 581.1$ ns and the numerical calculation using the snowplow model gives ~ 620 ns. These values are different from the simulation result, 603.0 ns as shown in Fig. 1(a). The snowplow energy equation[3] enables us to treat the reflection of the plasma column and estimate the radius of plasma column at pinch. As shown in Fig. 1(a), the prediction of pinch time and radius disagree with the simulation. Another defect of the snowplow model is that it cannot describe the shock front. The slug model[4] is capable of describing the shock front. The plasma radius and the position of the shock front in the slug model are governed by

$$\frac{dr_p}{dt} = \frac{1}{\left[\frac{2}{5} + \frac{3}{5}(r_s/r_p)^2\right]}\left[\frac{3}{4}\left(\frac{r_s}{r_p}\right)v_s - \frac{3}{5}\frac{\omega}{r_p}(r_s^2 - r_p^2)\right], \tag{7}$$

$$\frac{dr_s}{dt} = v_s, \qquad = \sqrt{\frac{8}{3}}\frac{1}{c\sqrt{4\pi\rho_0}}\frac{I(t)}{4\pi r_p}, \tag{8}$$

where r_p is the position of the plasma boundary, r_s that of the shock front, ρ_0 the initial mass density, and $2\pi/\omega$ the period of the plasma current $I(t)$. In Fig. 1(b), the simulation results are compared with the slug model and Fig. 1(c) shows the spatial distribution of density for different times, from which the appearance of the shock front can be noticed. There are conspicuous differences between the slug model and the simulation result. First of all, the predicted pinch time and radius are different. The slug model predicts that an equilibrium pinch is established when the shock front reaches the axis and there is no reflection of shock. But in the simulation, the plasma column is reflected after the pinch and then expands. The shock front is reflected after hitting the axis 50 ns before the pinch, finally disappearing just after the pinch.

The dynamics of temperature at axis are featured by the rapid change near the pinch, the higher ion temperature than the electron temperature and the two-step increase of temperature (Fig. 2). The evolutions of temperature and density are plotted in Fig. 3. To understand these dynamics in detail, the temporal variations at axis of the heating and cooling terms in Eq. (3) and Eq. (4) are investigated and depicted in Fig. 4.

In the compressional phase, up to about 550 ns, a shock is well developed [Fig. 1(c)] but the heating up to 10 eV is mainly caused by Joule heating, substantially ionizing carbons. So the ionization is a main cooling source in this phase. Another important phenomena is the diffusion of magnetic field leading to the broadening of the current shell (Fig. 5), which cannot be described by the analytical models. Recently, Foord *et al.*[22] experimentally observed an ionization wave propagating toward the axis in this phase. In their

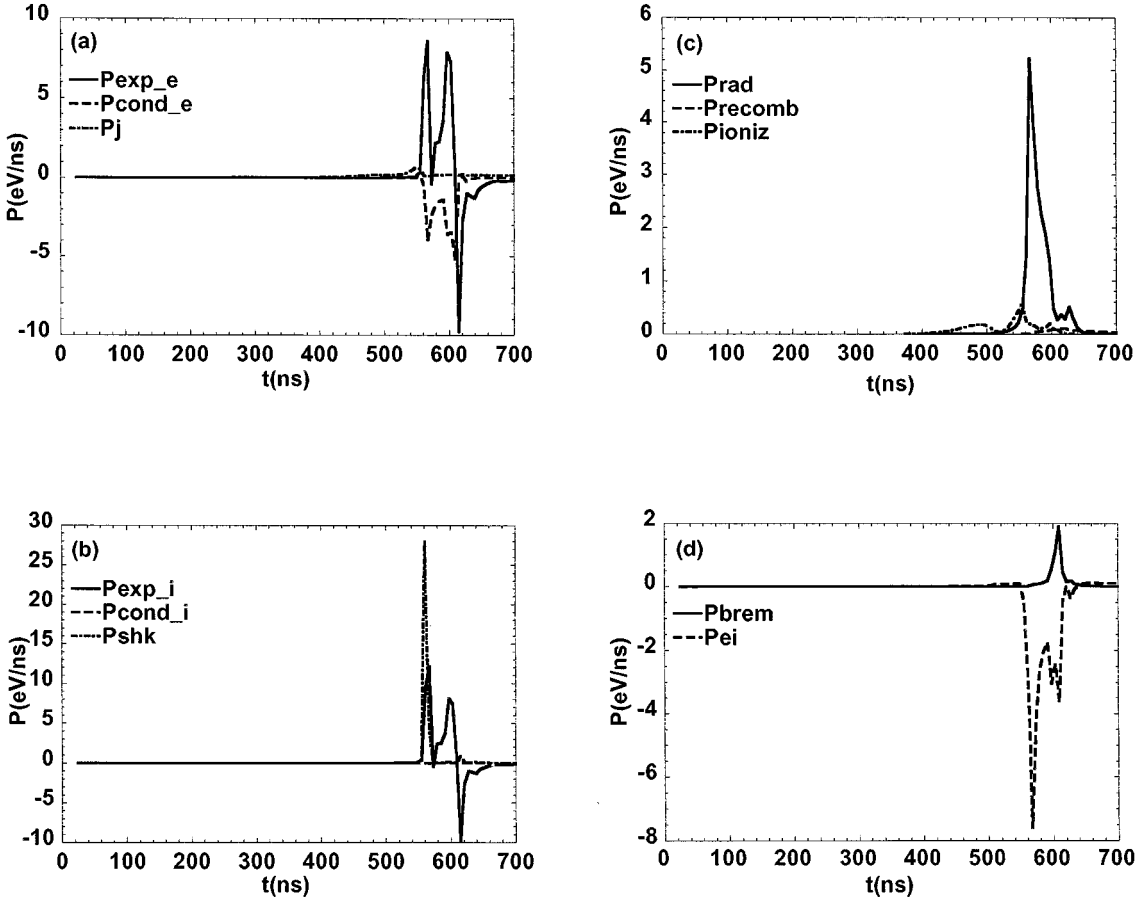

FIG. 4. The temporal variation at axis of the various heating and cooling terms appeared in Eq. (3) and Eq. (4). All quantities are in unit of eV/ns.

interpretation, the effect due to the magnetic diffusion was neglected; however, our preliminary simulation shows that the magnetic diffusion and Joule heating may play an important role in understanding the dynamics of the ionization wave. A further analysis of heat flow in the compressional phase is under current investigation.

At the time of the shock hitting the axis for the first time, t=560.8 ns [curve II in Fig. 1(b)], the ion shock heating power increases abruptly and the adiabatic heating follows immediately [Fig. 4(b)], leading to an jump of ion temperature up to 105.0 eV [Fig. 2(a)]. The higher adiabatic heating for ions than that for electrons and the shock heating cause the ion temperature to be higher than the electron temperature by 30 eV [Fig. 2(a)]. This difference disappeared in about 30 ns due to the electron-ion energy exchange. At this moment, radiation loss by the resonance transitions of C V and C VI ion reaches its maximum [Fig. 4(c)] which keeps the temperature from increasing further. Additional heating caused by adiabatic compression occurs at the time, $t = 597$ ns, when the reflected shock front collides with the compressing plasma boundary. This leads to another jump of ion temperature to 177.3 eV at 609.0 ns, 6 ns later after the pinch. The density at axis also reaches its maximum, $N_e = 3.8 \times 10^{20}\ \mathrm{cm}^{-3}$. Due to the high density, the electron-ion equilibration time, τ_{eq}, is so fast that the electron temperature almost exactly follows the ion temperature [Fig. 2(a)]. The heat conduction loss for electrons is also signifi-

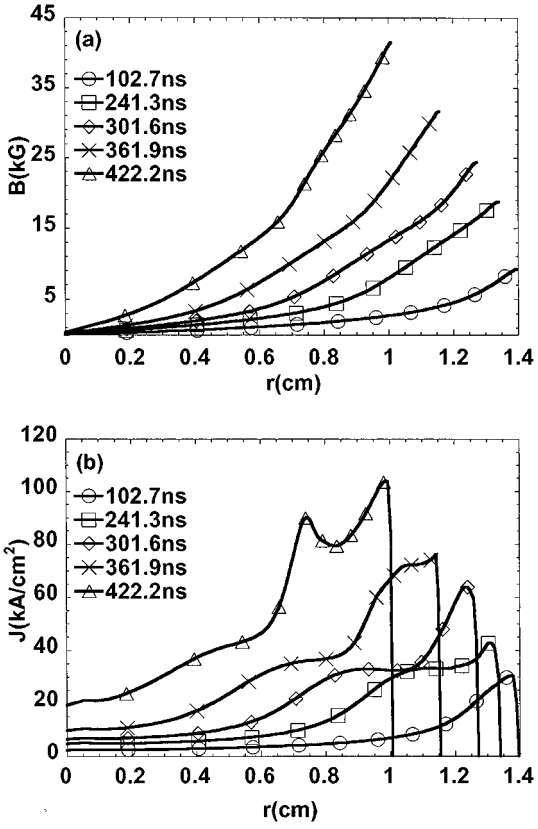

FIG. 5. The spatial distribution of (a) the magnetic field and (b) the current density in the compressional phase.

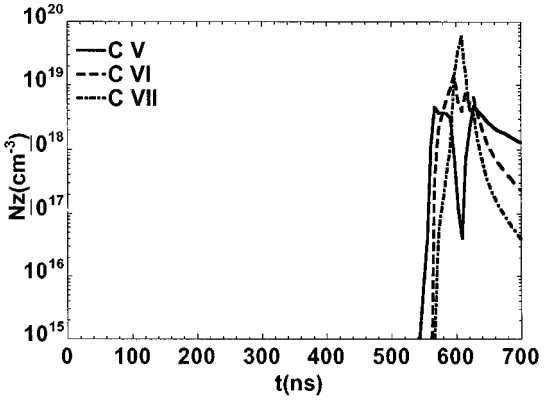

FIG. 6. The evolution of carbon ionization stages at axis.

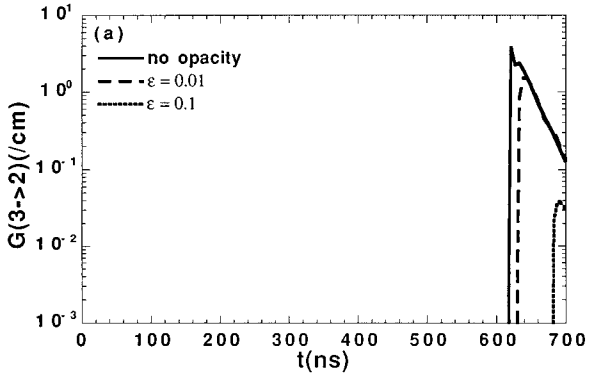

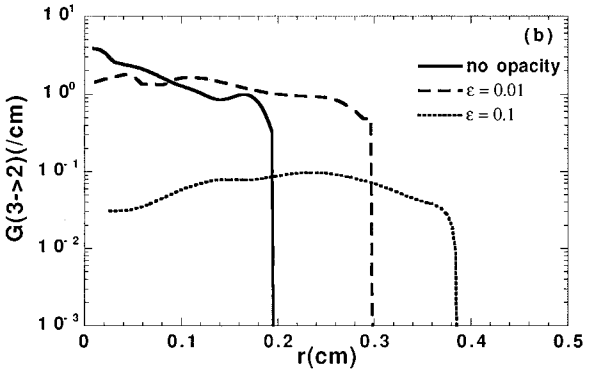

FIG. 7. The gains of H-like C VI Balmer-α line (18.2 nm) with different degrees of opacity: $\epsilon=0.0$ (optically thin), $\epsilon=0.01$ and $\epsilon=0.1$. (a) The temporal variation of the gain at axis. (b) The spatial distribution of the gain at the time of the maximum gain: 621.1 ns for $\epsilon=0.0$, 639.2 ns for $\epsilon=0.01$ and 690.5 ns for $\epsilon=0.1$.

cant but that for ions is negligible because $\kappa_{i\perp}/\kappa_{e\perp} \sim \sqrt{m_e/m_i}\,1/z^5 \sim 8.7\times10^{-7}$. The power loss by Bremsstrahlung radiation dramatically increases [Fig. 4(d)] because of its dependence on T_e and N_e as $P_{brem}\sim N_e^2 T_e^{1/2}$. But the radiation loss due to the resonance line is low since fully-stripped carbon ions are dominant [Fig. 6]. At the peak temperature, the thermal pressure is enormous, larger than the magnetic pressure and the plasma expands and cools down rapidly to 60 eV in 10 ns which leads to the strong recombination of C VII to H-like C VI ion. This heating and cooling mechanism is very similar to the experimental analysis of Hartmann's work.[23]

Since the recombination XUV laser requires the heating followed by the rapid cooling of plasma, the heat flow described above is very favorable to create the condition for recombination-pump XUV laser. The gain on H-like C VI Balmer-α (18.2 nm) has been calculated, solving the collisional-radiative model for excited level populations and using the following gain formula,[9]

$$G=\frac{1}{8\pi c}\frac{\lambda_{ul}}{\delta\lambda}g_u A_{ul}\left(\frac{N_u}{g_u}-\frac{N_l}{g_l}\right)\ \ \mathrm{cm}^{-1}, \tag{9}$$

where λ_{ul} is the wavelength of the lasing line (18.2 nm) and g the statistical weight of an atomic level, A_{ul} the spontaneous decay rate between the levels and N_u, N_l the population of the upper and lower lasing levels, respectively. For $\delta\lambda$, Doppler broadening is assumed:

$$\delta\lambda=\frac{2\lambda}{c}\sqrt{\frac{2T_i}{m_i}\ \ln 2},$$

where m_i is ion mass. Figure 7 shows the temporal variation of the gain at axis and the spatial distribution of the gain at the time of maximum gain in the case of an optically-thin plasma. The gain value, $G\simeq 3.8\ \ \mathrm{cm}^{-1}$ shows a chance to use the Z-pinch system for a recombination laser.

The gain on H-like C VI Balmer-α relies not only on the cascading processes followed by the three-body recombination but also on the fast depletion of the lower laser-level ($n=2$) population via Lyman-α transition. The reabsorption of the Lyman-α line can be detrimental to obtaining and maintaining gain. In a plasma which goes through dramatic dynamical changes as in our case, there may exist a strong velocity gradient ($\sim 10^7\ \mathrm{s}^{-1}$). The strong velocity gradient brings about the large Doppler shift of wavelength, resulting in the significant reduction of the opacity of the transition line.[24,25] However, the reduction of the opacity (τ) due to the velocity gradient was not large enough to bring the calculated gains and the experimentally-observed ones into agreement.[26,27] The anomaly factor ϵ, which is defined by

$$\tau_{eff}=\epsilon\tau_{actual},$$

was introduced to bring marginal agreements; however, its values used varied from 0.01 to 0.25 for different lasing conditions.[26]

In our simulation, τ_{actual} was calculated, using the methods suggested by Shestakov *et al.*[24] and Lee *et al.*[25] which take into account the Doppler shift due to the velocity gradient. The former is more appropriate for the strong velocity gradient (near pinch and expansion afterwards in our case) and the latter for the small velocity gradient (initial phase in our case). We also introduced the anomaly factor to see the effect of various degrees of the opacity. By the way of the escape probability method, the effect of the opacity was incorporated both into the calculation of the radiation loss in the hydrodynamics simulation and of the population in the population kinetics simulation. Figures 7 and 8 show the effects of the opacity. Figure 7 shows the behaviors of gain

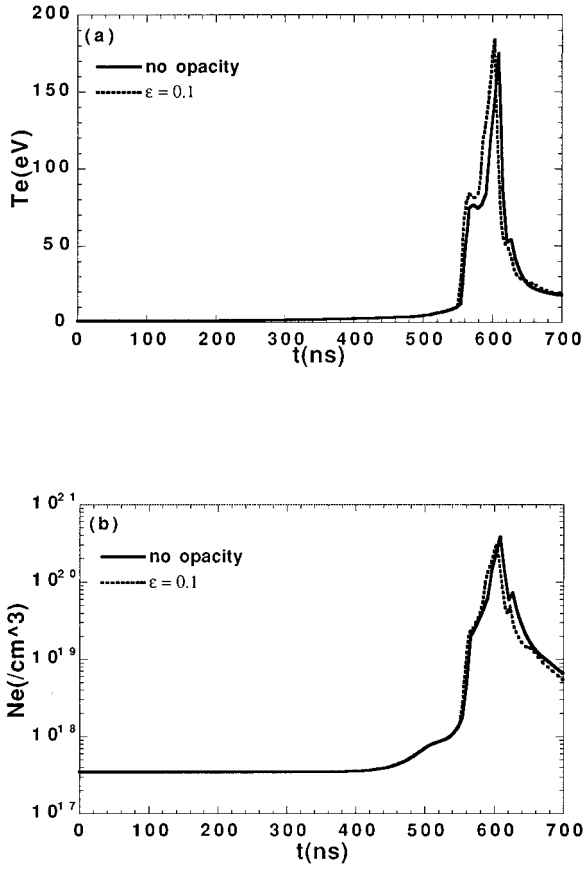

FIG. 8. The comparison between the hydrodynamics of no opacity and that of opacity with $\epsilon=0.1$. This shows the effect of opacity on hydrodynamics is very small for $\epsilon=0.1$. The temporal variation of (a) T_e and (b) N_e at axis.

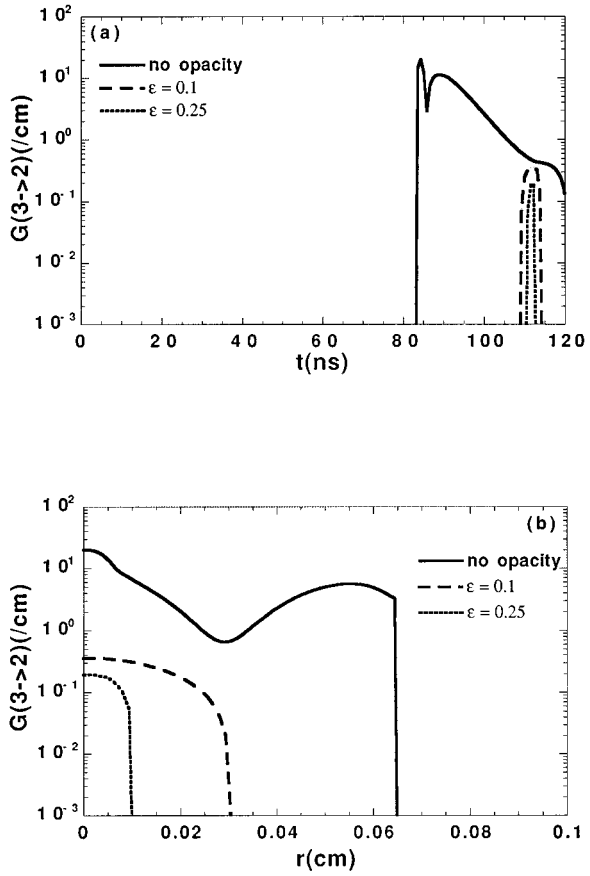

FIG. 9. The gains of H-like C VI Balmer-α line (18.2 nm) for a different set of initial parameters: $r_0=0.2$ cm, $N_0=2.5\times10^{18}$ cm^{-3}, $I_0=110$ kA and $(T/4)=100$ ns. The result also shows the effect of opacity. (a) The temporal variation of the gains at axis. (b) The spatial distributions of the gains at the time of the maximum gain: 84 ns for no opacity, 112 ns for $\epsilon=0.1$ and 112 ns for $\epsilon=0.25$.

without the opacity and with the opacity of $\epsilon=0.1$ and 0.01. With the increase of the opacity, the gain drops and comes later when the density is low and the opacity small. No gain is observed with the opacity of $\epsilon=0.25$. The time histories of the electron temperature and density at axis without the opacity and with the opacity of $\epsilon=0.1$ are shown in Fig. 8. Considering the case of the opacity of $\epsilon=0.1$, the effect of the opacity on the hydrodynamics is small but on the population kinetics is significant. We have performed a simulation for a different set of parameters: $r_0=0.2$ cm $N_0=2.5\times10^{18}$ cm^{-3}, $I_0=110$ kA and $T/4=100$ ns. The time history of gain at the axis and its spatial profile at the time of the maximum gain are shown in Figs. 9(a) and (b), respectively, for the different opacities (different anomaly factors). This set of parameters produces the better condition for lasing. The gain of 20 cm^{-1} is reached without the opacity and even for $\epsilon=0.25$, there exists the gain of 0.2 cm^{-1}. With the increase of the opacity, the gain not only drops and comes later but also its region becomes narrower from 600 to 100 μm.

In 1-D simulation as in our study, the uniformity along the axis is assumed. For the successful realization of soft x-ray laser, the uniformity along the axis is indeed of importance. Recently, several research groups were able to produce uniform plasmas and demonstrate the amplification of soft x-ray light. Hartmann *et al.* have produced homogeneous plasma columns in helium, and have computed that if such an experiment is scaled to carbon, a small signal gain of 2.1 cm^{-1} could be expected on 18.2 nm.[23] Rocca *et al.* also succeeded in obtaining the high amplification of Ne-like Ar IX 46.9 nm in a 12-cm-long Ar *Z*-pinch plasma[11] and observed the saturation of the intensity in a 15-cm-long Ar plasma.[28] Shin *et al.* have recently observed a small signal gain of $G\simeq2.8$ cm^{-1} on C VI 18.2 nm in a wall ablated capillary carbon plasma which is a *Z*-pinch plasma with different boundary conditions from those in the present study.[10] The *Z*-pinch dynamics with respect to the development of x-ray laser certainly deserves further study.

V. CONCLUSIONS

The global motion of *Z*-pinch carbon plasma can briefly be described by the analytical models but none of them can describe the dynamics in detail. The energy flow of the plasma has been studied using the one-dimensional MHD code in the cylindrical geometry with the ionization-balance equation. From the simulation, the dynamics of *Z*-pinch plasma is well described by the motion of plasma column and shock front. In the compressional phase, the plasma column is compressed toward the axis following the shock front which is well developed in this phase. This phase can also be characterized by the diffusion of magnetic field and Joule

heating. The hitting of the shock front on the axis followed by the stagnation of the plasma column rapidly increases the plasma temperature in two steps: first, by the ion shock heating and second, by the adiabatic compression. The plasma column then rapidly expands while the shock front fades away. The simulation also suggests that the rapid cooling of plasma by the adiabatic expansion may lead to adequate conditions for recombination XUV lasers. The effect of the opacity on the hydrodynamics and gain has also been studied, using the anomaly factor for the effective opacity and the escape probability method. The opacity has a more significant effect on gain than on the hydrodynamics. With the increase of opacity, the gain drops drastically and comes later in time.

ACKNOWLEDGMENTS

This work has been supported by the basic science program of Research Institute of Science and Technology 1994, the Basic Science Research Institute Program, Ministry of Education, 1994 (Project No. BSRI-94-2439), and Korea Science and Engineering Foundation (Contract No. 931-0200-022-2). Mr. K. T. Lee has been partially supported by the Young Investigator Program, Ministry of Education, 1994.

[1]J. S. Pearlman and J. C. Riordan, J. Vac. Sci. Technol. **19**, 1190 (1981); J. Bailey, Y. Ettinger, A. Fisher, and R. Feder, Appl. Phys. Lett. **40**, 33 (1982); T. N. Weinberg and A. Fisher, Appl. Phys. Lett. **47**, 1116 (1985); M. Howells, J. Kirz, D. Sayre, and G. Schmahl, Phys. Today **38**, 22 (1985); J. Kirz and H. Rarback, Rev. Sci. Instrum. **56**, 1 (1985).
[2]N. A. Krall and A. W. Trivelpiece, *Principles of Plasma Physics* (McGraw-Hill, New York, 1973), p. 123.
[3]T. Miyamoto, Nucl. Fusion **24**, 337 (1984).
[4]D. Potter, Nucl. Fusion **18**, 813 (1978).
[5]R. Courant and K. O. Friedrichs, *Supersonic Flow and Shock Waves* (Springer-Verlag, New York, 1948).
[6]D. Duston and J. J. Duderstadt, J. Appl. Phys. **49**, 4388 (1978).
[7]S. Maxon and T. Wainwright, Phys. Fluids **27**, 2535 (1984).
[8]V. N. Shlyaptsev, A. V. Gerusov, A. V. Vinogradov, J. J. Rocca, O. D. Cortazar, F. Tomasel, and B. Szapiro, in *Ultrashort Wavelength Lasers II*, edited by S. Suckewer, Proc. SPIE **2012**, 99 (1994).
[9]R. C. Elton, *X-ray Lasers* (Academic, New York, 1990), Chaps. 2 and 4.
[10]H. J. Shin, D. E. Kim, and T. N. Lee, Phys. Rev. E **50**, 1376 (1994).
[11]J. J. Rocca, V. Shlyaptsev, F. G. Tomasel, O. D. Cortazar, D. Hartshorn, and J. L. A. Chilla, Phys. Rev. Lett. **73**, 2192 (1994).
[12]R. L. Bowess and J. R. Wilson, *Numerical Modeling in Applied Physics and Astrophysics* (Jones and Bartlett, Boston, 1991), Chap. 4.
[13]D. Düchs and H. R. Griem, Phys. Fluids **9**, 1099 (1966).
[14]S. I. Braginskii, in *Review of Plasma Physics*, edited by M. A. Leontovich (Consultants Bureau, New York, 1965), Vol. 1, p. 216.
[15]L. Spitzer, *Physics of Fully Ionized Gases*, 2nd ed. (Wiley, New York, 1962), p. 148.
[16]W. Wiese, M. Smith, and B. M. Glennon, *Atomic Transition Probabilities* (U.S. Government Printing Office, Washington DC, 1966), Vol. I.
[17]R. W. P. McWhirter, in *Plasma Diagnostic Techniques*, edited by R. H. Huddlestone and S. L. Leonard (Academic, New York, 1965), Vol. 21, Chap. 5.
[18]N. H. Burnett and A. A. Offenberger, J. Appl. Phys. **45**, 2155 (1974).
[19]R. D. Richtmyer and K. W. Morton, *Difference Methods for Initial-Value Problems* (Interscience, New York, 1967).
[20]V. F. D'yachenko and V. S. Imshennik, in *Review of Plasma Physics*, edited by M. A. Leontovich (Plenum, New York, 1970), Vol. 5, p. 462.
[21]D. G. Carolan and V. A. Piotrowicz, Plasma Phys. **25**, 1065 (1983).
[22]M. G. Foord, Y. Maron, G. Davara, L. Gregorian, and A. Fisher, Phys. Rev. Lett. **72**, 3827 (1994).
[23]W. Hartmann, H. Bauer, J. Christiansen, K. Frank, H. Kuhn, M. Stetter, R. Tkotz, and T. Wagner, Appl. Phys. Lett. **58**, 2619 (1991).
[24]A. I. Shestakov and D. C. Eder, J. Quant. Spectrosc. Radiat. Transfer **42**, 483 (1989).
[25]Y. T. Lee, R. A. London, G. B. Zimmerman and P. L. Hagelstein, Phys. Fluids B **2**, 2731 (1990).
[26]G. J. Pert, in *X-ray Lasers 1990*, edited by G. J. Tallent (Institute of Physics, New York, 1990), p. 143.
[27]C. Chenais-Popovics, R. Corbett, C. J. Hooker, M. H. Key, G. P. Kiehn, C. L. S. Lewis, G. J. Pert, C. Regan, S. J. Rose, S. Sadaat, R. Smith, T. Tomie, and O. Willi, Phys. Rev. Lett. **59**, 2161 (1987).
[28]J. J. Rocca, M. C. Marconi, F. G. Tomasel, V. N. Shlyaptsev, J. L. A. Chilla, and D. P. Clark, in *Soft X-Ray Lasers and Applications*, edited by J. J. Rocca, P. L. Hagelstein, Proc. SPIE **2520**, 201 (1995).